Materials Science & Engineering A 824 (2021) 141808

Contents lists available at ScienceDirect

Materials Science & Engineering A

journal homepage: www.elsevier.com/locate/msea

Orientation dependent tensile properties of a selective-laser-melt 316L stainless steel

Mustafa Güden [a,*], Hakan Yavaş [b], Ahmet Alptuğ Tanrıkulu [b], Alper Taşdemirci [a], Barış Akın [c], Samed Enser [a], Ayberk Karakuş [a], Burcu Arslan Hamat [b]

[a] Dynamic Testing and Modelling Laboratory, İzmir Institute of Technology, İzmir, Turkey
[b] Turkish Aerospace Industries, Innovation Division, Ankara, Turkey
[c] Numesys, Numerical Systems, Istanbul, Turkey

ARTICLE INFO

Keywords:
Additive
SLM
316-L
Inclination angle
Modelling

ABSTRACT

The effect of specimen inclination angle with respect to building direction on the tensile properties of a selective laser melt 316L alloy was investigated. Tensile test specimens were fabricated with the angles between 0° to 90° at 15° intervals using a rotation scanning. In addition, 316L alloy test specimens were generated in the ANSYS 2020R1 additive module and tensile tested in LS-DYNA in order to determine the effect of residual stresses on the tensile strengths. The microscopic analysis revealed a strong ⟨110⟩ fiber texture orientation along the building direction (the loading axis of 0° inclined specimens) and a weak <111> texture or nearly random distribution of directions in the normal to the building direction (tensile loading axis of 90° inclined specimens). The yield and tensile strength increased and ductility decreased with increasing inclination angle. The strength variation with the inclination angle was shown well-fitted with the Tsai-Hill failure criterion. Although, the used numerical models indicated an inclination-dependent residual stress, the difference in the residual stresses was much lower than the difference in the strengths between 0° and 90° inclined specimens. Predictions showed a lower twinning stress in 0° inclined specimens due to ⟨110⟩ fiber texture orientation in the tensile axis. The fiber texture resulted in extensive twinning; hence, higher ductility and tension-compression asymmetry in 0° inclined specimens. Based on these results, the variations in the strength and ductility of tested SLM-316L specimens with the inclination angle was ascribed to the variations in the angle between the fiber texture orientation and loading axis.

1. Introduction

High corrosion and oxidation resistance, good plastic formability and biocompatibility with human body make stainless steel 316L one of the most preferred alloys for the applications involving corrosion and/or elevated temperature oxidation such as nuclear reactors, fluid transportation pipes, implants and prostheses [1]. There have been numerous review articles on Selective Laser Melt (SLM)-fabricated 316L (SLM-316L) alloy, summarizing the microstructure evolution and the microstructure-dependent mechanical properties [2–4]. The cooling rates in SLM have been reported extremely high (10^3–10^8 K/s) [5,6], causing not only the development of residual stresses [7–9] but also significant variations in the microstructure, mechanical properties and defects formed in the final product [3,10,11]. The microstructure of SLM-fabricated metallic alloys is also quite different from that of conventionally manufactured cast and wrought alloys [5]. SLM-316L alloy develops a microstructure composing of columnar grains aligned in the laser building direction and sub-grains of micro/nano size inter-grain cells (sub-grain) inside columnar grains [12–21]. A crystallographic fiber texture formation in which <100> directions aligned through building direction was commonly reported, while texture was tuned to <110> and <111> directions by using a small hatching spacing and a high laser power [20,22–26]. Previous studies have also reported a twin-induced-plasticity (TWIP) in SLM-316L as similar with TWIP steels [17,19,20,27]. The measured yield strengths were also higher than those of conventionally processed ones [19,28,29]. Anisotropy in the flow stress and ductility has also been reported; the flow stress is higher in normal to the building direction and the ductility is vice-verse [19,20]. The yield and tensile strengths and the ductility of SLM-316L sequentially ranged 450–590 MPa, 640–700 MPa and 36–59

* Corresponding author.
E-mail address: mustafaguden@iyte.edu.tr (M. Güden).

https://doi.org/10.1016/j.msea.2021.141808
Received 20 March 2021; Received in revised form 17 June 2021; Accepted 23 July 2021
Available online 27 July 2021

% and these were sequentially 160–365 MPa, 450–555 MPa and 30–43 % for conventional 316L [2].

The present study is a continuation of above studies and mainly focuses on the effect of specimen inclination on the tensile properties of SLM-316L alloy. For that, cylindrical SLM-316L bars with vertical inclinations to the building direction between 0° (vertical) to 90° (horizontal) at 15° intervals were fabricated using a multidirectional biaxial scanning laser pattern rotated 90° between adjacent layers (±45°). The Tsai-Hill failure criterion of anisotropic materials was fitted with the yield and tensile strengths in order to predict a relation between the strength and inclination angle. More, the test specimens were generated in the additive module of ANSYS 2020R1 using the same process parameters of the used SLM. Finally, the generated model test specimens were numerically tensile tested in LS-DYNA. The results of numerical models were used as guide to understand the experimentally detected anisotropy in the flow stresses of SLM-316L.

2. Experimental and numerical studies

2.1. Specimen preparation, tests and characterization

Tensile test specimens were processed in a Laser-powder bed fusion AM Concept Laser M2 Cusing device (400 W continuous wave fiber laser) using gas atomized 316L powder with an average size of 50 μm under a continuous flow of nitrogen. The power, scanning rate, hatching space and spot size of incident beam were sequentially 370 W, 900 mm s^{-1}, 115 μm and 160 μm. A multidirectional biaxial scanning laser pattern rotated 90° between adjacent layers was used to construct the specimens with a constant layer thickness of 30 μm. The energy density was calculated ~120 J mm^{-3} using power/(scanning rate x hatching space x layer thickness).

Initially, cylindrical SLM-316L bars, 6 mm in diameter and 80 mm in length, were fabricated with 90°, 75°, 60°, 45°, 30°, 15° and 0° to the building direction (z-axis) as shown in Fig. 1(a). The tensile test specimens were machined from these bars, coded as A-G in Fig. 1(a) (A refers to 90° inclined specimens and G to 0° inclined specimens). Fig. 1(b) shows the optical micrographs of the corresponding microstructures in the x-, y- and z-direction in 0° inclined SLM-316L specimen. As is seen,

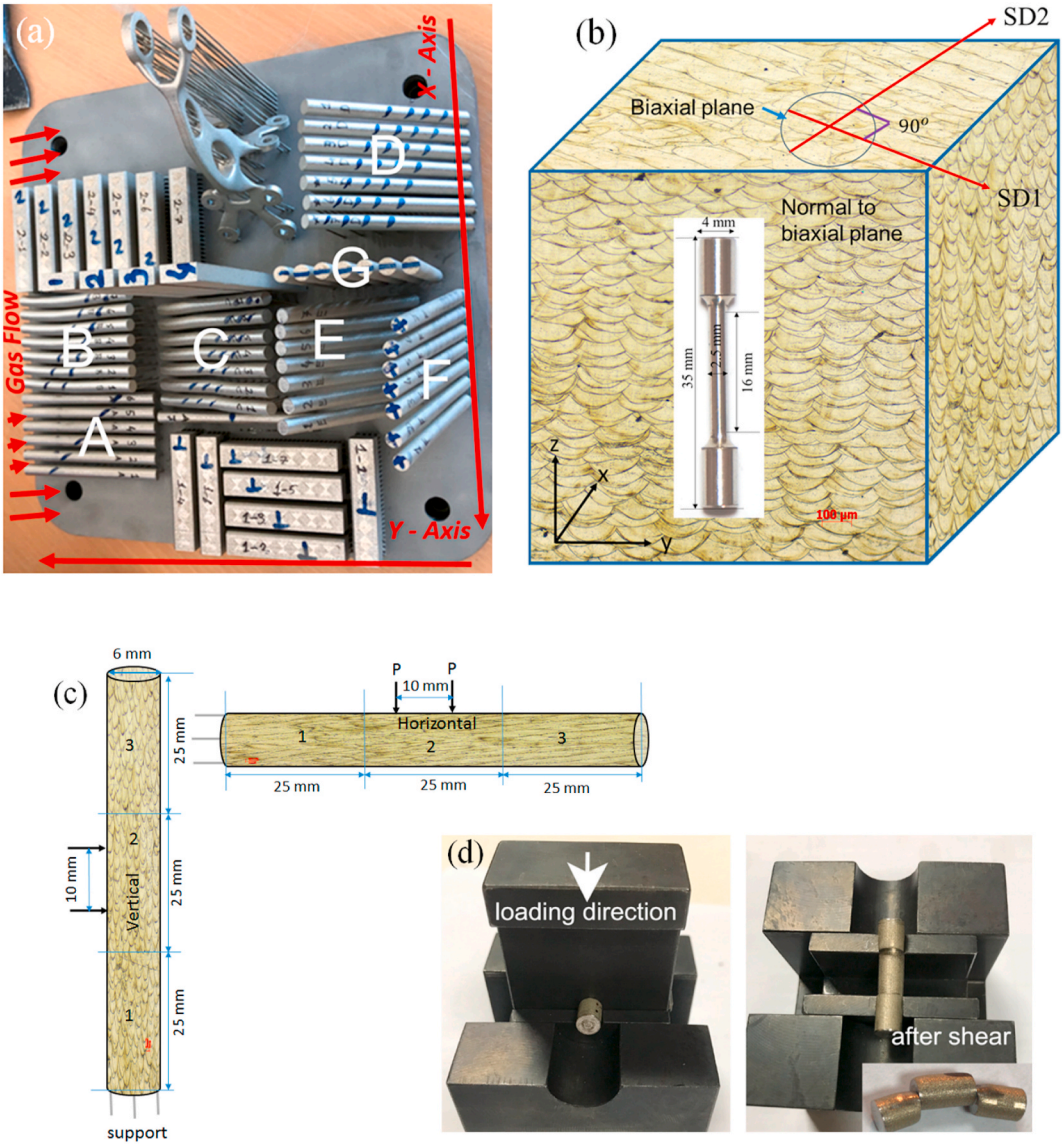

Fig. 1. The pictures (a) SLM-fabricated bars after cleaning, (b) the axis dependent microstructure of fabricated specimens and a 0° inclined tensile test specimen and (c) shear test specimens and (d) double shear test fixture and deformed specimen.

the microstructure in the x-y plane consists of biaxial (±45°) melt pools and the cross-sections of biaxial (±45°) melt pools are seen in the x-z and y-z planes. Two scanning directions (SD1 and SD2) are also shown in the same figure. Tensile test specimens were machined from as-built bars in accord with the ASTM E8/E8M−13a standard "Standard Test Methods for Tension Testing of Metallic Materials" with a gage-diameter of 2.5 mm and a gage-length of 16 mm (Fig. 1(b)). A picture of a tensile test specimen with 0° inclination is also shown in Fig. 1(b). Quasi-static tension tests were performed at a strain rate of $\sim 1 \times 10^{-3}$ s^{-1} in a Shimadzu AG-X universal test machine. At least three tests were performed for each group of specimens and the specimen displacements were recorded using a video extensometer. Double shear tests were performed in order to fit the Tsai-Hill failure criterion with the yield and ultimate tensile strengths of the investigated SLM-316L as function of inclination angle. Cylindrical shear test specimens were sliced from 6 mm-diameter and 80 mm-long bars into 25 mm-long bars using an electro discharge machine as shown in Fig. 1(c). Before slicing, the bar ends were removed by 2.5 mm. The shear tests were performed on the specimens with 0° (vertical) and 90° (horizontal) inclination to the building direction at a cross-head speed of 0.02 mm s^{-1} in a double shear test fixture based on the MIL-STD-1312/13A standard [30]. As shown in Fig. 1(c), 10 mm apart shear loads (P) are applied parallel to the y-direction in a vertically fabricated and parallel to the z-direction in a horizontally fabricated specimen. The pictures of the used test fixture together with a tested SLM-316L specimen are shown in Fig. 1(d).

The specimens for metallographic analysis were cut by using a precision diamond saw under a continuous flow of water. Mounted specimens were then grinded and polished down to 0.25 μm using diamond suspensions. The metallographic specimens were etched using a 10 % HNO_3, 20 % HCl and 20 % Glycerol solution. The microscopic analyses were performed in a Meiji IM7 100 optical microscope and FEI Quanta 205 FEG scanning electron microscope (SEM) with an electron backscattered diffraction (EBSD) system. The final polishing of the specimens for EBSD analysis were performed using a 100 nm alumina suspension. The raw data obtained from EBSD were analyzed using Atex software [31]. Hardness Vickers (HV) tests were performed on the polished and polished-etched surfaces of mounted specimens in a Shimadzu Micro Vickers Hardness Tester by applying a 19.61 N load for 10 ms. The crystallographic structures of as-built G and A specimens were determined using a Philips X'Pert Pro X-Ray Diffraction (XRD) device (Cu-Kα radiation, $\lambda = 1.54$ A° and 40 kV). The dislocation density of as-built specimens was measured using Williamson and Hall method [32]. Assuming the broadening of peaks (β) in an XRD pattern are due to grain size-broadening and strain-broadening, the following equation was used to calculate β[32].

$$\beta - \beta_{ins} = \delta_{hkl} Cos\theta_{hkl} = \frac{\lambda}{D} + 4\varepsilon sin\theta_{hkl} \tag{1}$$

where, λ, D, ε, δ_{hkl}, θ_{hkl} and $\beta_{ins}$are the XRD wavelength (0.154 nm), the specimen grain size and residual strain, the broadening of full width at half maximum (*FWHM*) of diffraction peak, the diffraction angle and the broadening of instrument, respectively. The broadening of the used instrument, β_{ins}, was determined through the XRD of an unstrained Si powder and determined 0.38. The slope of $FWHM\ Cos\theta_{hkl}$ versus $4\sin\theta_{hkl}$ curve gives the residual strain as [32].

$$\varepsilon = \frac{FWHM\ Cos\theta_{hkl}}{4\ sin\theta_{hkl}} \tag{2}$$

The dislocation density(ρ_d) was then calculated using the following equation [33].

$$\rho_d = k\frac{\varepsilon^2}{b^2} \tag{3}$$

where, k is a constant, 16.1 for FCC and b is the Burgers' vector, 2.55×10^{-10} m for FCC iron [33]. The density of SLM-316L was determined by the Archimedes' method. Five repeating measurements were made and the results were then averaged. The density of bulk 316L was determined from a commercial annealed-extruded Viraj Impoexpo 316L bar.

The strengthening of dislocation density was calculated using the Taylor equation [34],

$$\Delta\sigma = M\alpha G b\sqrt{\rho} \tag{4}$$

where M is the Taylor factor (2.9), α is an empirical constant (0.23) and G is the shear modulus (65 GPa) [35,36]. Assuming the mechanical properties is isotropic in the x- and y-axis, the Tsai-Hill failure criterion is [37],

$$\left(\frac{\sigma_z}{\sigma_z^*}\right)^2 - \left(\frac{\sigma_z\sigma_y}{\sigma_z^*}\right)^2 + \left(\frac{\sigma_y}{\sigma_y^*}\right)^2 + \left(\frac{\tau_{yz}}{\tau_{yz}^*}\right)^2 = 1 \tag{5}$$

where, z-axis is taken as the building direction and σ_z^*, σ_y^* and τ_{xz}^* are sequentially the failure strengths in the z- and y-axis and the shear strength in the z-y plane. Then, the off-axis failure strength, $\sigma(\theta)$, is formulated as [37].

$$\sigma(\theta) = \left(\frac{cos^2\theta(cos^2\theta - sin^2\theta)}{\sigma_z^{*2}} + \frac{Sin^4\theta}{\sigma_y^{*2}} + \frac{(cos^2\theta sin^2\theta)}{\tau_{yz}^{*2}}\right)^{-1/2} \tag{6}$$

where, θ is the inclination angle.

2.2. Numerical model of SLM and tensile tests

The numerical generation of SLM-316L cylindrical bar specimen was carried out using the additive module of ANSYS 2020R1 [64]. Specimen geometry was defined in the SpaceClaim 2020R1, then ANSYS Workbench Additive Manufacturing tool (thermomechanical) was activated. The numerical generation consists of three stages; first, a transient thermal solver by defining the characteristics of 3D printer including the laser heat input effects, second, a static solver to calculate the structural and thermal stresses and strains during specimen building, then third, base removal was done. In the simulation of the manufacturing, the build process is modeled layer by layer solidification of the layers in the part. Thermal (temperature related) and structural (mechanical distortion and stress related) physics are largely uncoupled and there is a weak coupling occurs. Thus, the thermal phenomena can be simulated first layer-wise and by using the temperature related data simulation continues with the structural part. In the model, elements are added over time. First the part is meshed with a layered mesh and then the regular element birth and death strategy is followed to activate element layers to mimic the build process. In addition, the boundary conditions are constantly altered for the convection surfaces. In ANSYS, the method followed to simulate the whole structure is called lumped layer approach. In this method thermal and structural physics are uncoupled and it is assumed that the thermal effects in the built direction are more significant than those in the in-plane direction. Thus, several powder layers are lumped to a single finite element layer. The powder is assumed to have the same physical and mechanical properties along all directions. A constant heat transfer coefficient is assumed between the powder and the environment. 316L was also used a base material in the numerical models. The baseplate only serves as a heat sink. In the thermal analysis, the base plate was assumed to be at 100 °C, and cool down temperature was selected as 22 °C. In the structural analysis, the bottom surface was fixed fully.

A layered Cartesian mesh methodology was followed in the analysis within specimen building stage. A projection factor of 0 was selected to obtain uniform mesh sizing and good quality of mesh. However, this method has certain disadvantages including the weakness in capturing the curved surfaces of the geometry if the number of elements is not sufficient. Along the height of the specimen, global coordinate system projection was kept constant to obtain a constant mesh height in the layering direction. Solid185 3D 8-node structural elements were used in

the mesh generation. For the base removal, "ekill" command was used to remove the base elements and to prevent instability issues the specimen was fixed at its both ends. Once the solution is done, stresses and strains (normal, shear, elastic, plastic and equivalent) were exported within the global coordinate system.

To investigate the effect of residual stress and strain on the mechanical behavior of the material, the quasi-static tension test was modeled in LS-DYNA [65]. For this purpose, the deformed geometry exported from ANSYS was meshed with sweeping in a butterfly mesh pattern. During this stage initial stresses and strains calculated at the post-process of ANSYS were mapped to the newly meshed geometry. Finally, fixed support boundary condition was applied at both ends of the specimen. In the end, a static solve was conducted to obtain the final condition of the specimen. The stress data of all elements along every direction at each Gaussian point calculated and collected with *INITIAL_STRESS_SOLID card of LS-DYNA. With the methodology explained above, it was possible to obtain an explicit type of mesh including initial stress data and deformed shape. The quasi-static tension tests were modeled using LSDYNA 971 R11. Specimen was modeled with solid elements. *MAT_PLASTIC_KINEMATIC material model was used for the constitutive behavior of the material with the flowing parameters taken from ANSYS library: density = 7950 kg m^{-3}, elastic modulus = 195 GPa, Poisson's' ratio = 0.25, yield strength = 225 MPa, tangent modulus = 2091 MPa and failure strain = 0.5. The boundary prescribed motion card was defined for the top end of the specimen and the bottom end was fixed fully in order to prevent the motion along the axial direction. Mass scaling methodology was followed, the deformation rate was increased while the density of the specimen was decreased until the kinetic energy to internal energy ratio was kept below 5 %. Since only the specimen was modeled explicitly there was no contact algorithm defined. The optimum number of elements for both numerical simulations was determined by doing a mesh sensitivity analysis. The mesh sensitivity analysis revealed that an element size of 0.5 mm resulted to the solutions within an acceptable calculation time.

3. Results and discussion

3.1. Microstructural characterization

The average density was determined 7821 ± 5 kg m^{-3} from the as-built vertical SLM-316L bars (specimens G). The average density of C316-L bar specimen (20 mm diameter and 10 mm length) was determined 7838.5 ± 5 kg m^{-3}. Using these two density values, the porosity of SLM-316L was determined 0.22 %. The determined porosity level is noted to be in accord with a recent study which reported a relative density over 99.5 % for an SLM-316L alloy processed using the similar processing parameters [38].

The optical micrograph showing the microstructure of a 90° inclined specimen normal to the building direction (in the tensile loading y-axis) is shown in Fig. 2(a). Columnar-like grains across the melt pools is clearly seen in this micrograph. The use of rotation scanning strategy results in a mismatch in the positions of melt layers and leads to the development of interrupted grains as shown by the dashed lines in Fig. 2 (b). Therefore, the melt pools in the present 316L alloy resemblance overlapping semi ellipses rather than nail-top appearance as seen in Fig. 2(a). Part of the columnar-like grains have the lengths the same as the thickness of melt pools and part have the lengths several times that of the melt pools (Fig. 2(b)). The average width of the columnar grains was measured by the linear intercept method by counting 164 grains and determined 29.27 μm (15–45 μm). Within the melt pools inside the columnar-like grains, a cellular microstructure/sub-structure development is also seen in Fig. 2(b) (combined optical and SEM micrographs). The sub-grain resemble 5–6 sided honeycomb-like structure and are oriented in-plane and out of plane inside the columnar grains as shown by the arrows in Fig. 2(b). Both the thermal gradient development in the building direction and the re-melting of scanned layers were proposed to affect the orientation of sub-grain [39]. The sub-grain are the regions of high dislocation density (dislocation network) with higher heavy atoms concentrations of Cr and Mo arising from the extremely fast cooling rates impeding the diffusion [12,28]. The widths of sub-grain were measured using an image program on the SEM pictures. Total 100 cells were counted and an average size of 1.05 ± 0.22 μm (0.7–1.67 μm) was determined. Small size precipitates (~100 nm) are also seen at the edge/corner of the sub-grain, an example is shown by a circle in the inset of Fig. 2(b). These precipitates were reported amorphous chromium-containing silicate nano inclusions and formed due to the high oxygen affinity of Si and Cr at high temperatures [12].

Fig. 3(a) shows the EBSD maps of 0° and 90° inclined specimens normal in tensile axis (x-y plane for 0° inclined specimen and z-x plane for 90° inclined specimen), respectively. Previously, a strong fiber texture of ⟨110⟩ along the build direction (z-axis) and a weak ⟨111⟩ texture or random distribution of directions along the normal to the building direction (x- and y-axis, ±45° to the scanning directions) of a SLM processed 316L specimen were shown for rotating scanning [40]. A similar fiber texture is also found in the present study. A strong <110> fiber texture along the building direction (in the tensile loading axis of 0° inclined specimens), while a weak ⟨111⟩ texture or nearly random distribution of directions are seen in the x- and y-axis (in the tensile loading axis of 90° inclined specimens) as depicted in Fig. 3(b) and (c). Fig. 3(d) schematically shows the orientation of <110> fiber texture with the inclination angle of the tested specimens. The average grain sizes in the biaxial plane and normal to the biaxial plane are sequentially

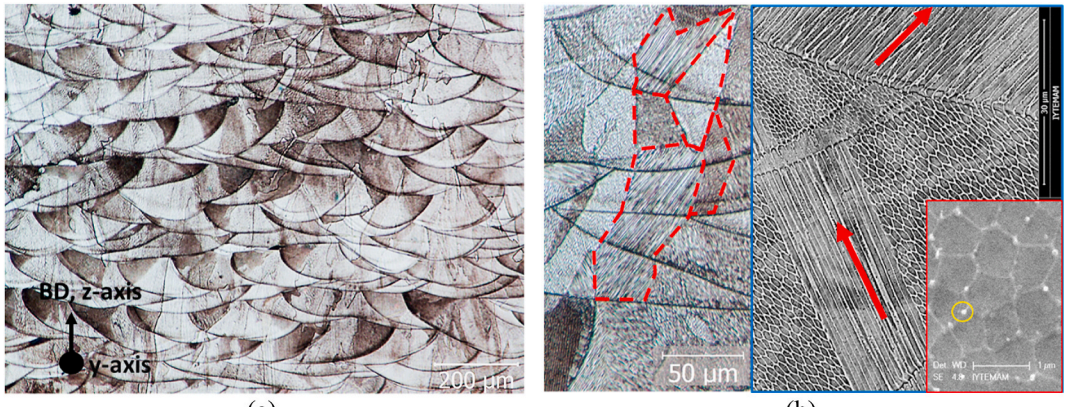

Fig. 2. The micrographs of an SLM-316L 90° inclined specimen normal to the building direction (in the tensile loading y-axis) showing (a) melt pools and (b) columnar grains, sub-grain orientations an precipitates at the corners of sub-grain (circle).

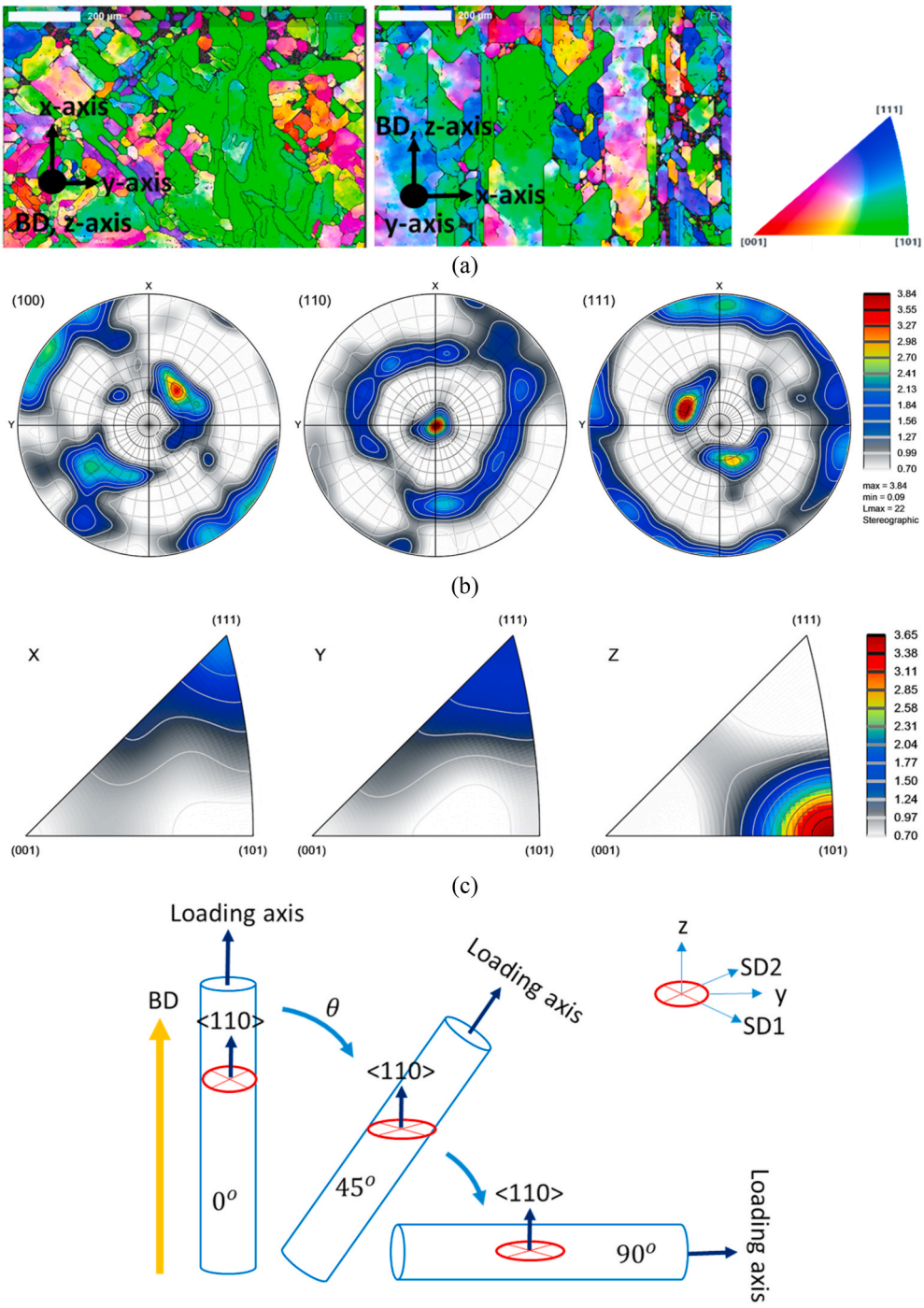

Fig. 3. (a) EBSD maps in the tensile axis of 0° and 90° inclined specimens, (b) pole figures for 0° inclined specimen normal to building direction (normal to z-axis), (c) inverse pole figures showing <110> fiber texture in the z-axis and (d) the schematic of fiber texture orientation and tensile loading axis as function of inclination angle.

determined 32.5 and 22 μm in the EBSD analysis, which are comparable with the grain size measured using optical microscope.

The average hardness in the y-direction (10 tests) was determined 220.5 ± 4.7 HV, while the average hardness in the z-direction was slightly lower, 214.1 ± 2.4 HV. The average flow strengths were predicted ~720 and 700 MPa for the y- and z-direction using HV (MPa)/3, respectively. The hardness tests showed parallel lines around the indentations, which were determined slip lines as the re-polishing and etching the specimen removed these lines (see Supplementary Figs. 1(a) and (b)).

The XRD of an as-built G specimen shown in Fig. 4 further confirms a fully austenitic structure. The residual strain based on the Williamson and Hall method is found 0.23 % (shown in the inset) and the corresponding dislocation density using Eqn. (3) is 1.3 × 10^{15} m^{-2}. A lower dislocation density, 1.18 × 10^{15} m^{-2}, was previously reported for an SLM-316L as-built specimen which was fabricated using a multidirectional biaxial scanning laser pattern rotated 70° between adjacent layers [41]. Another study reported also a similar dislocation density, ~1.14 × 10^{15} m^{-2}, for an SLM-316L alloy processed using a bidirectional scanning pattern at a laser energy density of 100 J mm^{-3} [19] which is smaller than that of the present study (120 J mm^{-3}). The higher dislocation density found in the present study may be because of a high laser

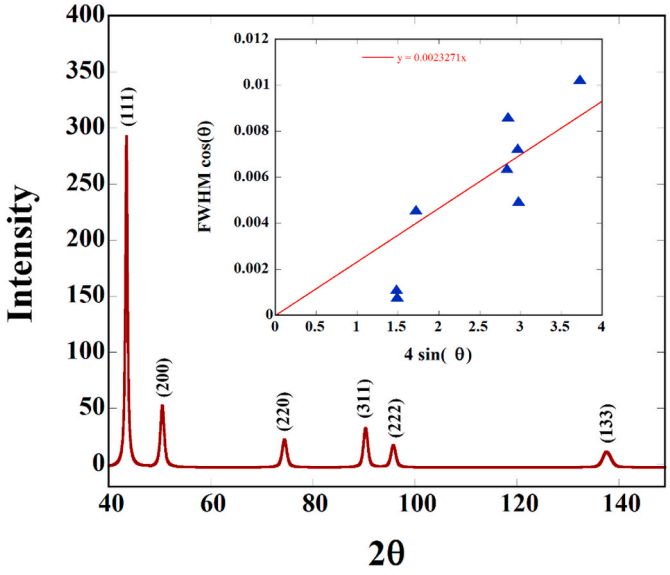

Fig. 4. The XRD pattern and calculated residual strain of SLM-316L (specimen G and A together).

energy density used. By taking the average dislocation density of C316-L alloy 3.8 × 10^{14} m^{-2} [42], the dislocation density strengthening was determined 315 MPa based on Eqn. (4). Relatively high yield strength of the studied SLM-316L alloy as compared with conventional 316L alloy may be therefore due to the process-inherited relatively high dislocation density.

3.2. Quasi-static tension and shear tests and failure stress criterion

Fig. 5(a) and (b) show the engineering and true stress-strain curves of three tests of 0° and 90° inclined specimens, respectively. True stresses after necking in these curves are not valid and merely shown for comparison. As is seen, the stress-strain curves of three tests of the same group of specimens are very similar to each other, except there are slight differences in the engineering fracture strains. The stress-strain curves of 15°, 30°, 45°, 60° and 75° inclined specimens were also repeatable (not shown here). A long plateau region (uniform elongation region) is found between the yield (0.004–0.006) and ultimate tensile strains (0.55–0.75) in the engineering stress-strain curves of all tested specimens. In order to demonstrate the global deformation and fracture characteristics of the tested SLM-316L specimens, the video-captured pictures of 0° and 90° inclined test specimens before and after necking are sequentially shown in Fig. 5(a) and (b). As is seen, the uniform elongation region is followed by necking at the mid-section of the test specimens and eventually the specimens fracture at the necking region. Although, the engineering fracture strains range 0.55–0.75 in Fig. 5 (a–c), the true fracture strains are much higher than these as will be elaborated in the next sections. Fig. 5(c) shows the representative true stress-strain and true strain hardening-strain curves of the specimens with 0° and 90° inclinations. The true ultimate tensile strengths and true uniform strains were determined from these curves using the Considere's rule, $\frac{d\sigma}{d\varepsilon} = \sigma$. The determined true tensile strengths and true uniform strains of 0° and 90° inclined specimens by using Considere's rule are marked and shown Fig. 5(c); the true uniform strains and true ultimate strengths are 0.51 and 990 MPa and 0.4 and 1051 MPa for 0° and 90° inclined specimens, respectively. In the same figure, the predicted twinning stresses, 643 and 800 MPa for 0° and 90° inclined specimens, are also shown, which will be elaborated later.

Fig. 6(a) shows the representative true stress-strain and true strain hardening-strain curves of the specimens with different orientations. Note that the lowest strain hardening is exhibited by 0° and 15° inclined

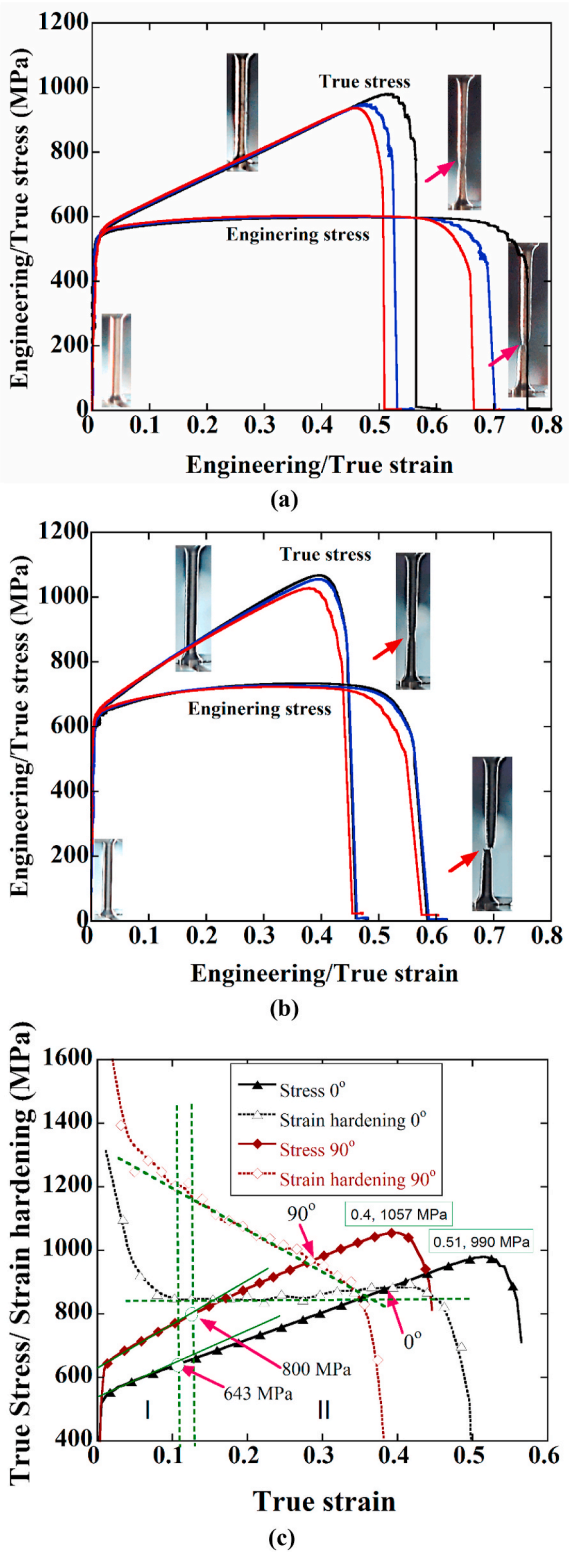

Fig. 5. The engineering and true stress-strain curves of 3 specimens of (a) 0° and (b) 90° inclined specimens and (c) the corresponding true-strass-strain and strain hardening-strain curves and the determined true ultimate tensile strengths and true uniform strains by Considere's rule.

specimens and the highest by 75° and 90° inclined specimens. The strain hardening of 30°-60° inclined specimens is intermediate. The variations of 0.2 % proof strength, true flow stress at 10 % strain, true ultimate tensile strength and uniform strain with inclination angle are shown in

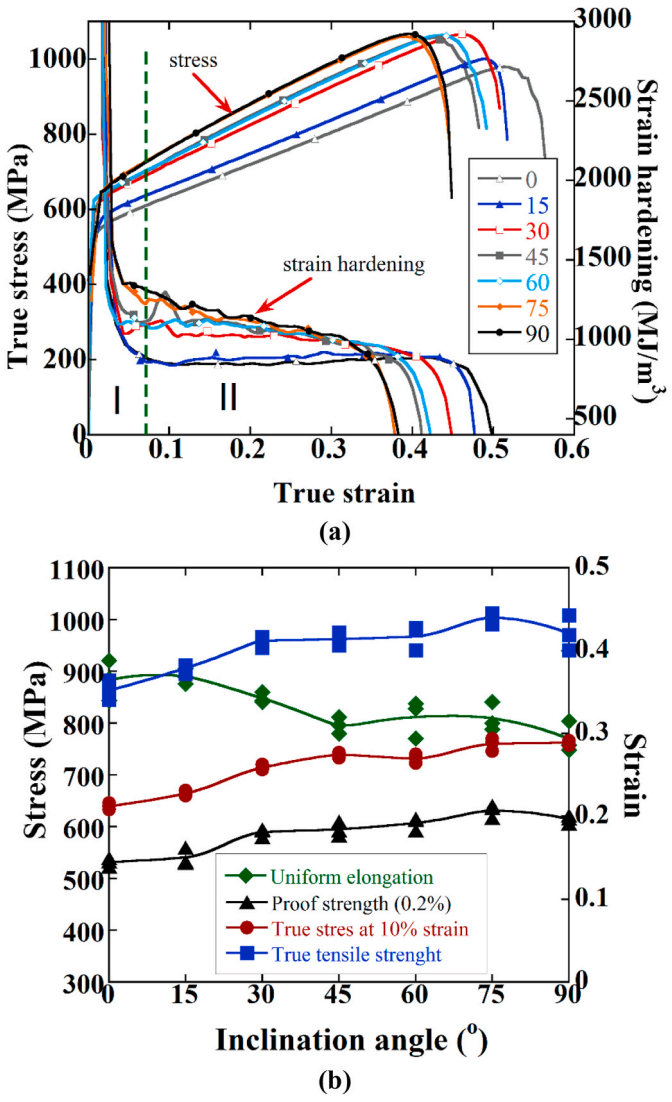

Fig. 6. (a) Representative true stress-stress and strain hardening-strain curves at 0°-90° and (b) the variations of proof strength, true stress at 10 % strain, true tensile strength and uniform strain with inclination angle.

Fig. 6(b). As is seen, the proof strength, 10 % strain-flow stress and true tensile strengths increase as the inclination angle increases from 0° to 45°; thereafter, they remain almost constant at increasing angles except 75° inclined specimens show slightly higher flow stress and tensile strength than 90° inclined specimen. On the other side, the uniform true strain is highest in 0° and 15° inclined specimens and decreases as the inclination angle increases from 0° to 45°; thereafter, it also remains constant between 45° and 90° except 90° inclined specimens exhibit slightly lower uniform strains. Regardless the inclination angle, SLM-316L specimens exhibit relatively high uniform strains (0.35–0.45) and high engineering fracture strains (0.5–0.75), indicating a relatively high ductile tensile deformation behavior.

Fig. 7(a) shows the shear stress-displacement curves of three horizontal (H) and vertical (V) double shear test specimens. The shear tests are repeatable and the specimens deformed until about large displacements without any fracture as seen in the pictures of the deformed specimens in the inset of Fig. 7(a). The representative shear stress-displacement curves of each specimen (the shear stress of V specimens is shifted in the displacement) are shown Fig. 7(b). The maximum shear stresses in these curves are considered as the shear strength and the proportional limits as the shear yield strength. The average shear strength of horizontal specimens (90° inclined specimens), 540 MPa

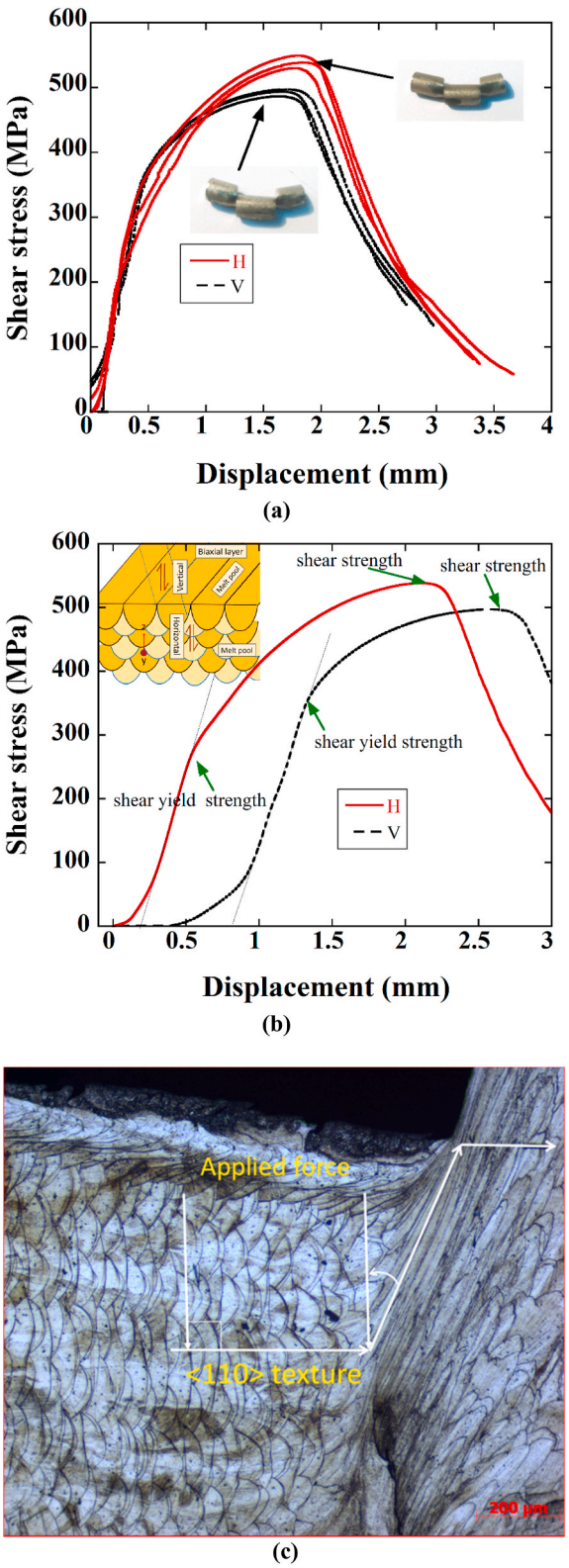

Fig. 7. (a) Shear stress versus displacement curves of vertical and horizontal specimens, (b) the representative curves and the determination of shear yield strength and shear strength (H: horizontal and V: vertical) and (c) optical micrograph showing the reorientation of fiber texture in the shear deformation zone in a vertical specimen.

(530–550 MPa), is slightly higher than that of vertical specimens (0° inclined specimens), 493.6 MPa (488–498 MPa). However the average shear yield strength of vertical specimens, 358.3 MPa (354–366 MPa), is higher than that of horizontal specimens, 256.7 MPa (226–288 MPa). The anisotropy is also seen in the shear strength properties when the shear load applied parallel to the melt pools (vertical) and normal to the melt pools (horizontal). Shear loading parallel to the fiber texture orientation (<110>) induces lower slip and twining deformation stresses and normal to the fiber texture orientation (random) is opposite (will be elaborated later). In the vertical specimens, the applied shear force is normal to the fiber texture orientation initially; hence, the yield stress is higher, while the shear deformation reorients the texture along the loading axis as depicted in Fig. 7(c), resulting in lower shear strength. In the horizontal specimens, the loading direction is parallel to the fiber texture orientation; hence, the initial yield strength is lower; but the applied shear load increases the angle between loading axis and texture orientation, resulting in higher shear strengths.

The experimental strength values used to fit Eqn. (6) are tabulated in Table 1. The results of fitting of proof strength and UTS with Eqn. (6) are shown in Fig. 8. The off-axis strengths of the investigated SLM-316L specimens are seen in Fig. 8 to be well predicted by using the Tsai-Hill failure criterion.

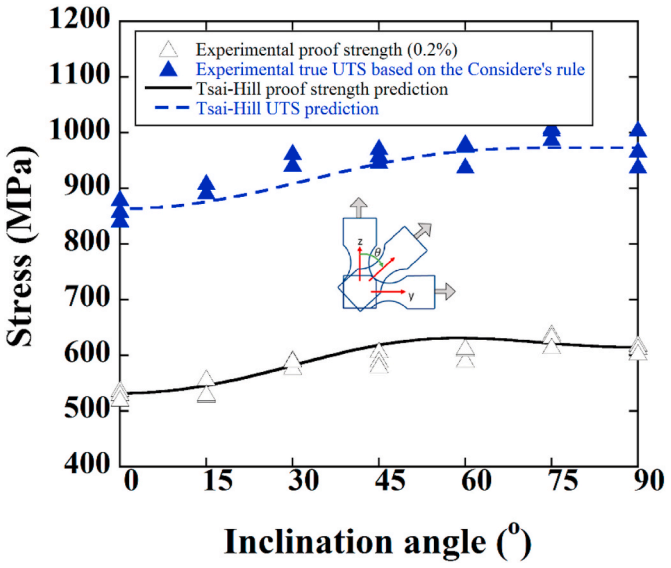

Fig. 8. The fitting the experimental strength values with the Tsai-Hill failure criterion.

3.3. Deformation characteristics of tested specimens

All tensile tested specimens exhibited TWIP. The previously proposed localized twinning in certain regions on a very fine scale [43] was also observed. Fig. 9(a) and (b) show the optical micrographs of the twinned regions (away from the necking) of the fractured tensile specimens with 0° and 90° inclinations, respectively. The twins seen in the marked regions of the same micrographs are inclined to the loading axis and the localized twinning is evident with the formation of the steps at the melt pool boundaries. The number and the thickness of the localized twin regions of 0° inclined specimens were higher those of 90° inclined specimens. The SEM observations showed that the distance between individual twins was less than 100 nm, smaller than the sub-grain size, 1.05 μm.

The optical micrographs of the polished-etched cross-section of 0° and 90° inclined tensile test specimens at and away from the necking region (uniform strain region) are shown in Fig. 10(a) and (b), respectively. The hardness test indentations and the measured diameters of the specimens in the uniform strain and necking regions are also shown in the same micrographs. The true strains at the uniform strain region and fracture strength were calculated using the measured diameters of the uniform strain and necking regions by using $2ln\frac{d_o}{d}$;where sequentially d_o and d are the initial and measured diameters, respectively. The true uniform and true fracture strains were determined sequentially 0.55 and 1.48 (1.9 and 1.19 mm) and 0.45 and 1.32 (2 and 1.29 mm) for 0° and 90° inclined specimens, respectively. These also prove a higher ductility of 0° inclined specimens and very high true fracture strains of the tested SLM-316L specimens, over 1.3. Microscopically the determined uniform strains also differ only about 10 % from the measured ones, 0.51 and 0.4 for 0° and 90° inclined specimens, respectively. The corresponding HV values in the uniform strain and necking regions (5 tests in each) and the flow stresses calculated using HV (MPa)/3 are further tabulated in Table 2. Note that flow stresses determined by the hardness test increases from 700 MPa to 997.3 MPa in 0° inclined specimen and from 720 to 1055 MPa in 90° inclined specimen when the strain increases from yield to the strain at which necking starts. As tabulated in the same table, the determined flow stresses in the uniform strain regions are also comparable with the ones determined from the stress-strain curves (Fig. 5(c)), 990 and 1057 MPa for 0° and 90° inclined specimens, respectively. With the increase of deformation further in the necking region, the flow stress increases to 1215 and 1192 MPa sequentially for 0° and 90° inclined specimens (Table 2). These show significant strain hardening in the necking region, while the predicted fracture strength of 0° inclined specimen is higher than that of 90° inclined specimen. These results should be however taken cautiously as the strength determined by the hardness test may change locally. Note that the melt pools are extended and aligned in the loading axis near the fracture in both specimens. The pre-existent pores are also extended/elongated as shown inside the boxes in Fig. 10(a) and (b).

Table 1
The experimental strength values fitted with Eqn. 6

	σ_z (0° inclined specimen) (MPa)	σ_y(90° inclined specimen) (MPa)	τ(0°) V (MPa)	τ(90°) H (MPa)
Proof strength	532.1 (523–540)	614.7 (606–622)	358.3 (354–366)	256.7 (226–288)
True UTS (Considere's rule)	863.3 (845–883)	973 (941–1008)	493.6 (488–498)	540 (530–550)

All tested specimens showed a ductile fracture surface, largely composed of dimpled regions as depicted in Fig. 11 for a 0° inclined specimen. The measured dimple sizes ranged 0.3–1 μm and were nearly the same for all inclination angles. Randomly distributed holes in varying diameters (3–40 μm) were also seen on the facture surface (the inset of Fig. 11). The size and number of holes were determined smallest in 0° inclined specimen (~8 μm) and highest in 45° inclined specimen (~35 μm). It is presumed that these holes are formed by the tensile loading of partially fused particles and also the pre-existent holes. A recent study using μ-CT has shown a higher number of pore formation in 45° inclined SLM-316L specimen as compared with 0° and 90° inclined specimens [39], which is fully in accord with the present observation. A small attached partially melt particle inside a hole is seen in Fig. 11. The size of the particle is 2.74 μm (satellite of a larger particle) and the tensile pulling the particle results in smears on the hole-surface. Although not shown here the double shear test specimens also showed TWIP behavior as with the tensile test specimens. These specimens formed shear banding under the action of shear forces and heavy twin formation was observed near the shear band.

3.4. Numerical models

The SLM model residual stress counters of the cross-sections of

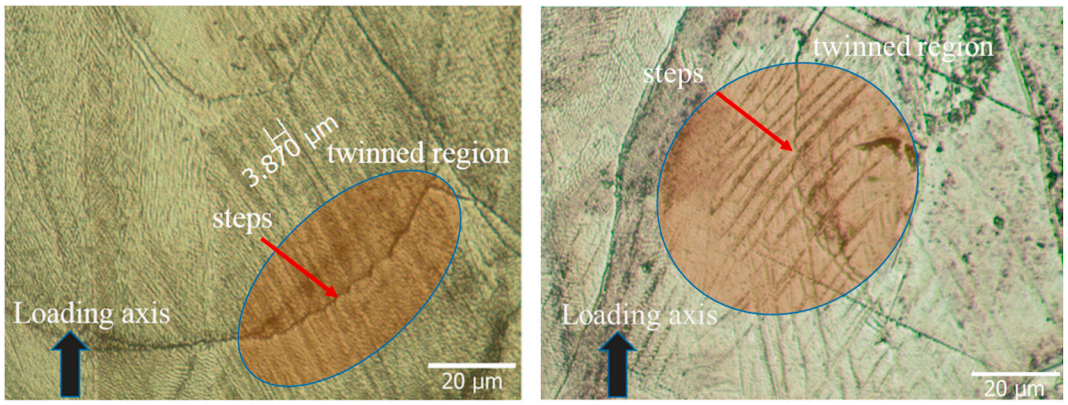

Fig. 9. Optical micrographs of the tensile tested specimens showing twinned regions and steps on the melt pool boundaries in the specimen with (a)0 and (b) 90° inclination.

Table 2
HV values of tensile tested 316 L specimens and the corresponding flow stresses.

	HV-0° Uniform strain region	HV-90° Uniform strain region	HV-0° Necking region	HV-90° Necking region
Mean	305	322.9	371.5	364.5
SD	5.68	2.98	6.15	6.61
Flow stress (MPa)	997.3	1055	1215	1192

cylindrical 0°-90° inclined specimens along the loading axis are sequentially shown in Fig. 12(a–f). Numerical models shown in the same figures clearly indicate the highest compressive residual stress development in the center of the specimen with 0° inclination (Fig. 12(a)) and the lowest compression residual stress in the specimens with 75° and 90° inclination. The compressive residual stress at the mid-sections of 0° inclined specimen reaches 550 MPa (Fig. 12(a)), while the central residual compressive stress in 90° inclined specimen is less than half of that, 180 MPa (Fig. 12(f)). The residual stress distribution of the AM Inconel 718 and Ti–6Al–4V parts was previously investigated numerically [44]. It was shown that the longitudinal residual stresses exhibited a steep gradient at both ends of the part and the through thickness stress

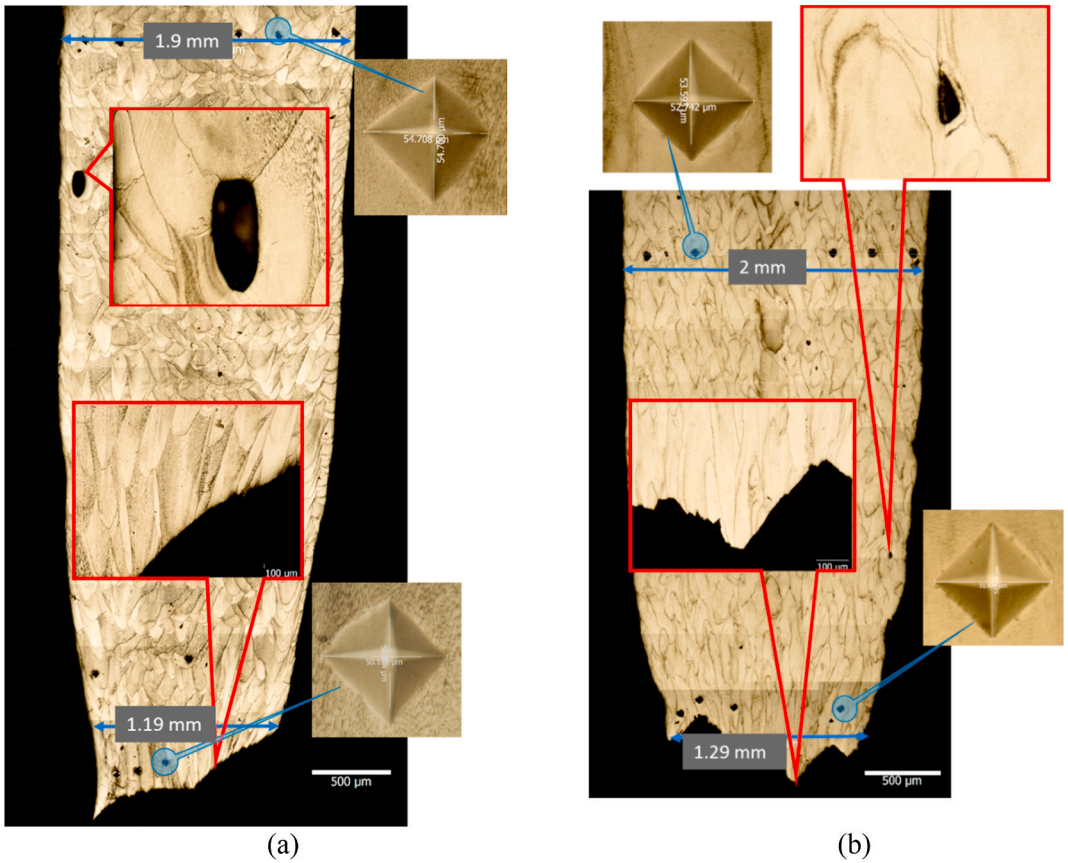

Fig. 10. Optical micrographs of the polished-etched cross-section of fractured tensile test specimens with (a) 0° and (b) 90° inclination.

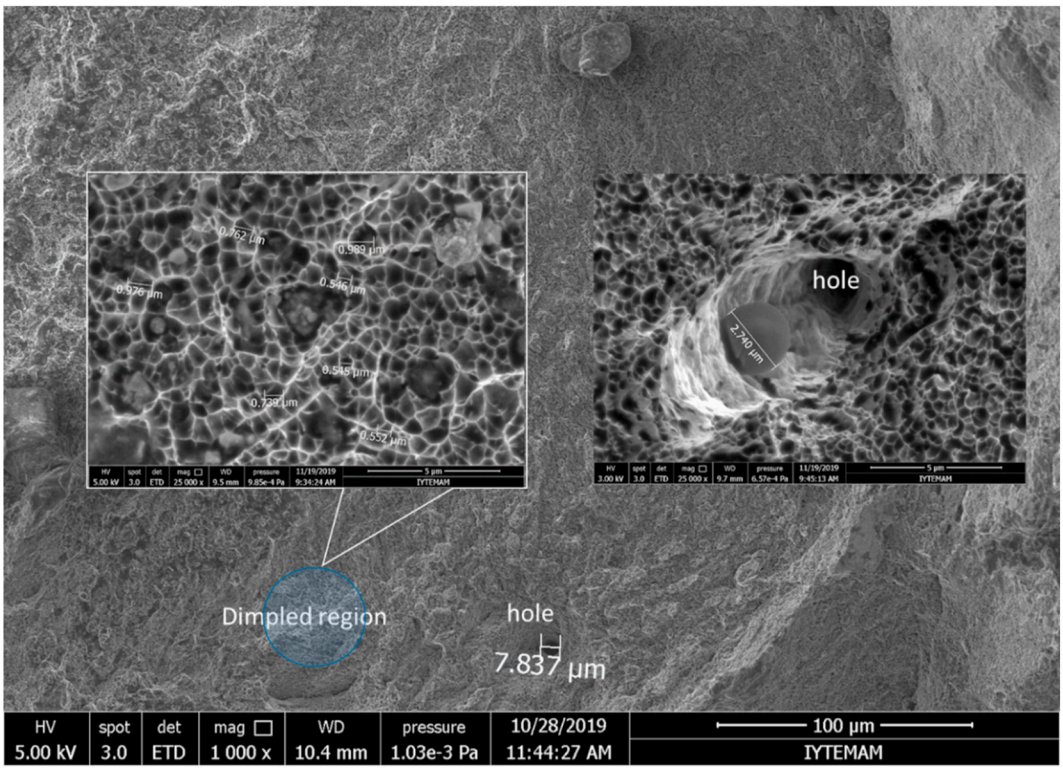

Fig. 11. The SEM micrograph of the facture surface of a 0° inclined specimen with dimpled regions and holes.

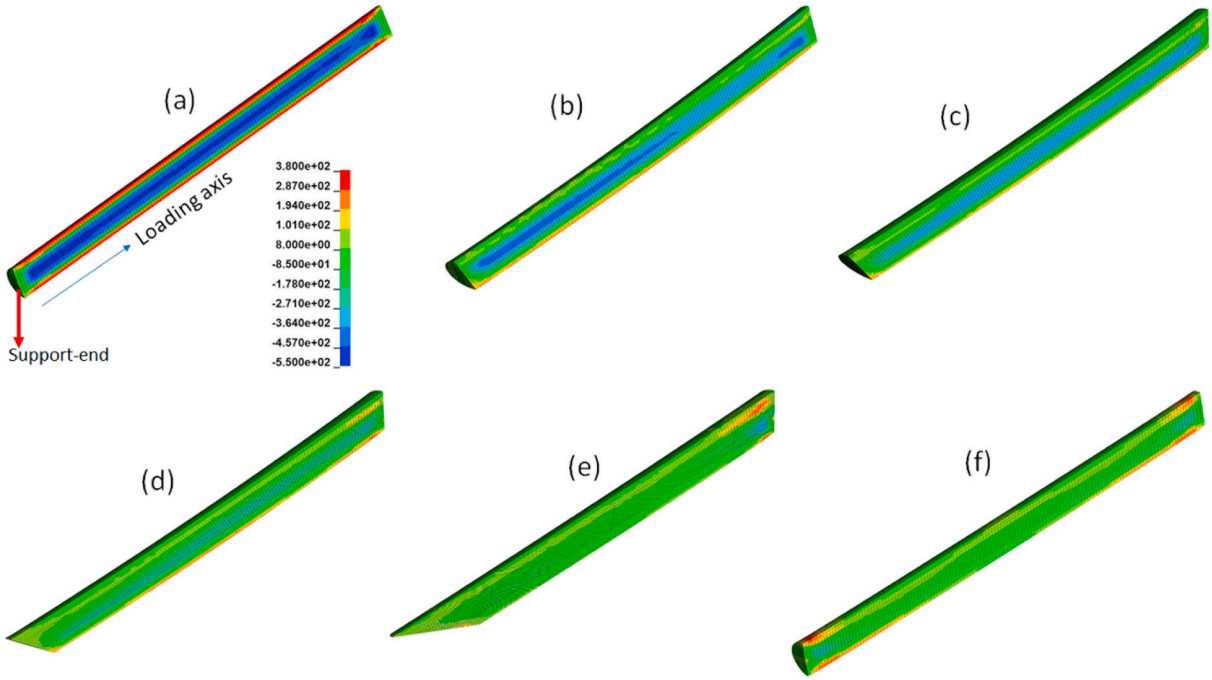

Fig. 12. Cross-sectional views of the cylindrical specimens of SLM model, showing the residual stresses along the loading axis in the specimens with the inclination angle of (a)0°, (b) 30°, (c) 45°, (d) 60°, (e) 75° and (f) 90.°.

changed abruptly at the base part interface. The residual stress also changed from tensile to compressive at the layer interfaces.

Fig. 13(a) shows true stress-strain curves of model specimens at increasing inclinations. The same as the experiments, the numerical stresses increases with increasing inclination angle. The same grouping of the experimental stress-strain curves can also be applied to numerical stress-strain curves regarding the similarity of the stress-strain curves as (1)0° and 15° (2)30°- 60° and (3)75° and 90° inclinations. Although the numerical variation of flow stresses with inclination angle is similar with the experiments, the experimental stress difference between 0° and 90° inclined specimens at 10 % strain is ~141 MPa, while this difference decreases to 31 MPa in the model.

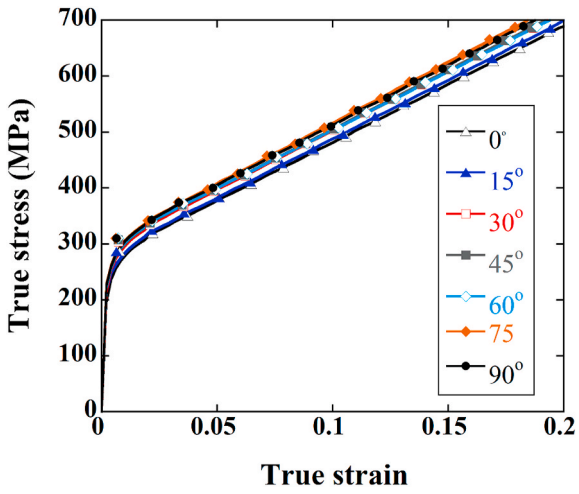

Fig. 13. Model true stress-strain curves at different inclination angles.

3.5. Anisotropy and texture

The mechanical properties of SLM fabricated alloys depend on the development of microstructure during processing, in which a laser-melt bed layer epitaxially solidifies on partially melt or previously solidified layers. The solidification front progresses either planar, cellular, columnar dendritic or aqua-axed dendritic depending on the growth and solidification rate, undercooling and solute diffusion coefficient [4]. The solidification takes place in certain crystallographic orientations in a direction thermal gradients grow faster. By considering the highest solidification rate in the directions of the most closed packed planes [15], the columnar dendritic grains are expected to orient in <100> direction in a FCC structure [45]. This results in a strong single crystal-like texture development in the laser scanning direction, leading to an anisotropy between normal and parallel to building direction. The mechanical properties of vertically and horizontally built Ti64V and 316L specimens, for example, exhibited different mechanical properties based on the difference in the texture development [40,46–49]. The texture development along the building direction was shown not only dependent on the processing parameters but also heat flow direction and the former grains orientations [45]. As stated earlier, the scanning strategy also affected the texture orientation and the use of rotation scanning strategy results in a strong <110> fiber texture along the building direction [40].

The observed anisotropy in the yield and tensile strength with the inclination angle may be due to the several factors, including the differences in the size of the sub-grain, volume and size of porosities, the magnitude of residual stress and texture development. A Hall-Petch relation was previously proposed between the sub-grain size and tensile strength of an SLM-316L [18,50]. While, other studies reported sub-grain as soft obstacles for the dislocation motion [28,51]. The SEM observations indicated similar sub-grain sizes for 0° and 90° inclined specimens. The low porosity levels of SLM-316L specimens (less than 0.5 %) processed using the rotation scanning strategy were also detected previously [19,40]. Since the rotation scanning repairs the defects between the adjacent scanning tracks in the previous layer [4], it induces a strong bonding and a reduced porosity and residual stress between the successive layers [52–54]. Although, the used numerical test models indicated an inclination-dependent residual stress development, the difference in the residual stresses was much lower than the difference in the strengths between 0° and 90° inclined specimens. By considering above, the residual stress is not considered as the major factor for the detected anisotropy in the yield and tensile strength with the inclination angle in this work.

The formation of mechanical twins depends on the stacking fault energy (SFE) and the applied stress (also strain) [55]. The typical range of SFEs for stainless steels was reported >45 mJ m^{-2} for dislocation slip, 20–45 mJ m^{-2} for twining and <20 mJ m^{-2} for martensitic transformation [27]. The lower values of SFE induces a large separation between the Shockley partials which prevents the cross-slip [56]. Twinning occurs when the resolved shear stress in the twining plane reaches a critical resolved shear stress in the twinning direction as similar with slip [43]. The critical twinning stress (σ_{TW}) is given by the following relation [36].

$$\sigma_{TW} = \frac{2\gamma_{eff}}{m_{TW} b_1} \tag{7}$$

where, γ_{eff} is the effective SFE, m_{TW} is the Schmid factor for the deformation twinning and b_1 is the Burgers vector of a partial dislocation. In FCC materials, the stacking faults are formed by the dissociation of a/2<110> unit dislocations into leading and trailing Shockley partial dislocations, a/6<211> (a is the lattice constant). The value of b_1 is therefore $\frac{a}{\sqrt{6}}$ (0.01.45 nm [36]). The effective SFE is given as [57,58].

$$\gamma_{eff} = \gamma_{sf} + \frac{(m_2 - m_1)}{2}\sigma b_1 \tag{8}$$

where, γ_{sf} is the SFE without applying stress (before deformation), σ is the applied stress and m_1 and m_2 are sequentially the Schmid factor for the leading ([121]) and ([$\bar{1}$12]) trailing partial dislocations [59]. When $m_1 > m_2$, the dislocations will be widely separated with a decrease in γ_{eff} and when $m_2 > m_1$, γ_{eff} will increase. The Schmid factors and number of deformation systems for slip and twinning (leading and trailing partial dislocations) are tabulated in Table 3 for a single crystalline in different loading directions under tension and compression. Note also that γ_{eff} varies with strain and its value was reported 20.8 mJ m^{-2} above 0.2 strain for a tensile tested SLM-316L [27]. Another study reported a value of 27 mJ m^{-2} for commonly used SLM powders [20], calculated using the formula developed in Ref. [60]. By taking γ_{eff} = 20.8 mJ m^{-2} and m_{TW} = 0.38 (average Shmid factor for twinning calculated using Atex software, see Supplementary Fig. 2), σ_{TW} is calculated 735 MPa for <110> texture orientation loading, 0° inclined specimens. By taking the Schmid factor for random orientation 0.326 [36], the σ_{TW} is calculated 880 MPa for 90° inclined specimens. Twinning was reported to start after the deformation by slip [43,61] by forming an abrupt change in the strain hardening curve. The stresses corresponding to the abrupt change in the strain hardening curves in Fig. 5(c) are therefore considered as the twinning stresses. The region I of Figs. 5(c) and 6(a) presumably is due to the deformation by slip and the region II is the deformation by slip and twinning. The twinning stresses determined by above method are 643 and 800 MPa (Fig. 5(c)) for 0° and 90° inclined specimens, respectively. Although the calculated and determined twinning stresses differ about 80–92 MPa, the difference between the calculated and determined

Table 3
The Schmid factors and number of systems for slip and twins of leading and trailing partial dislocations in single crystals, adapted from [62].

Loading axis	Schmid factor Tension				Compression	
	Slip	Twins	Partials		Partials	
			trail	lead	trail	lead
<100>	0.408	0.23	0.471	0.235	0.235	0.471
Number of systems	8	8				
$(m_2 - m_1)/2$			positive		negative	
<111>	0.28	0.31	0.16	0.31	0.31	0.16
Number of systems	6	3				
$(m_2 - m_1)/2$			negative		positive	
<110>	0.408	0.471	0.235	0.471	0.471	0.235
Number of systems	4	6				
$(m_2 - m_1)/2$			negative		positive	

twinning stresses of 0° and 90° inclined specimens is very much similar and sequentially 145 and 157 MPa.

Furthermore, twinning is polarized. In the materials without a texture, the twinning stress for tension and compression is similar, while in textured materials an asymmetry in the stresses between compression and tension tests is found [43]. For example, HCP materials with a strong fiber texture of basal plane through the loading axis favor the twinning in compression but not in tension [43]. The asymmetry is determined by the second term of Eqn. (8), $(m_2 - m_1)/2$. As tabulated in Table 3, this term is negative for tension and positive for compression for loading in <110> orientation (see Supplementary Fig. 3). Therefore, γ_{eff} will be lower in tension than compression in the fiber textured 0° inclined specimens based on Eqn. (8).

Fig. 14 shows the representative compression true stress-strain curves of 0° and 90° inclined specimens. The compression test specimens were extracted from the rectangular vertical and horizontal built specimens, which allowed the compression loading in the transverse direction (x-axis). As noted in the same figure, the fiber texture in the building direction induces a same yield stress in tension and compression, while the flow stress in compression increases more rapidly than tension. The higher compression strain hardening in the z-axis is mainly due to the change of deformation from slip and twinning in tension to a slip dominant one in compression. Both yield and flow stresses are however very similar in tension and compression in the y-axis. The anisotropy in the tested specimens are also seen in the deformed shapes of the tension and compression test specimens. The tension tested specimens in the z-axis results in almost circular facture surface cross-section and the specimens with 45° and 90° inclination display an elliptical facture surface cross-section as seen in the top pictures of Fig. 14. The arrows in the same picture are the z-axis or fiber texture orientation. A picture of a cylindrical compression test specimen (5 mm in diameter and length) extracted from a vertically built rectangular specimen is shown in the figure. The specimen was tested through the y-axis and the final deformed shape seen in the same figure is elongated through the z-axis (0.4 true strain). The deformed pictures of cubic test specimens extracted from a horizontally built rectangular specimen tested both y- and z-axis are also shown in the same figure. The anisotropy is clearly seen in these specimens also. Note that the specimens tested in the z-axis deformed until about large strains (0.7) without any fracture (tested-z in Fig. 14).

The favored twinning in the building direction results in higher true fracture strains than the normal to the building direction. Twinning delays the onset of necking by changing the strain hardening behavior. The higher ductility also results in a higher true fracture strength in the building direction (Table 2). The detected variations in the strength and ductility of SLM-316L alloy with the inclination angle is ascribed to the change of the angle between fiber texture direction and loading axis. The asymmetry may also be partly raised by the residual stresses. But, a compressive residual stress will induce a higher tensile yield stress and a lower compressive yield stress. Therefore, it is concluded that texture played a dominant in the detected asymmetry. Lastly, the Tsai-Hill failure criterion which is widely used to determine the failure of fiber reinforced composites in finite element modelling was shown applicable to the off-axis strengths of the studied fiber textured SLM-316L alloy.

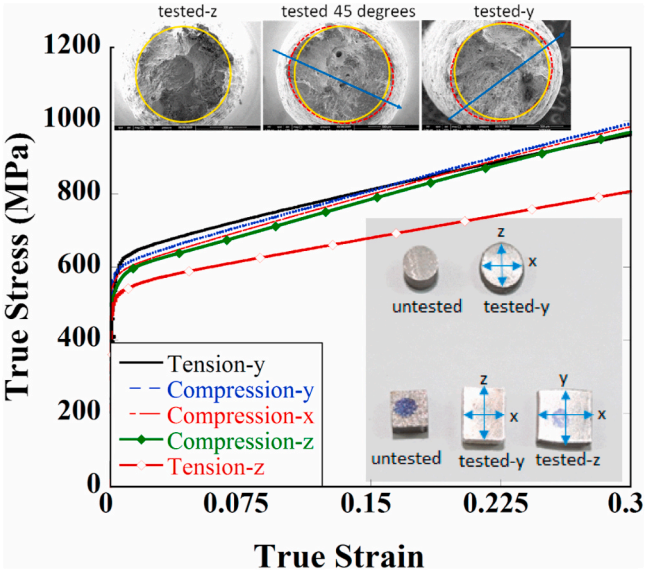

Fig. 14. The tensile and compression true stress-strain curves in the y and z-axis and compression true stress-strain curve in the x-axis.

4. Conclusions

The tensile behavior of 316L specimens processed using the rotation scanning strategy with an inclination angle to the building direction were experimentally investigated. An accompanying numerical processing model was also conducted and the processed model specimens were tensile tested as with the experiments. The microscopic analysis have shown that the used rotation scanning strategy induced a strong ⟨110⟩ fiber texture along the building direction and a weak ⟨111⟩ texture or nearly random distribution of directions in the normal to the building direction. The microscopic analysis of the tensile tested specimens indicated twinning-induced plasticity. The specimens with 90° and 75° inclinations exhibited the highest yield and tensile strengths, while the specimen with 0° inclination showed the highest fracture strain. The proof strength and UTS values were further fitted with the Tsai-Hill failure criterion in order to predict the off-axis strengths. The twinning stresses for 0° and 90° inclined specimens were further predicted based on the detected texture. The result have shown that the strong fiber texture orientation in the tensile loading axis of 0° inclined specimens resulted in a lower twinning stress, a higher ductility and an asymmetry in tension and compression stress-strain, while the near random distribution directions in 90° inclined specimens induced a higher twinning stress, a lower ductility and a similar stress-strain in tension and compression. On the other side, the used numerical model in the present study revealed the largest compressive residual stresses development in 0° inclined specimens. But, the difference in the residual stresses was much lower than the difference in the strengths between 0° and 90° inclined specimens. Therefore, the detected variations of the strength and ductility of SLM-316L alloy with the inclination angle was ascribed to the change of the angle between fiber texture orientation and loading axis.

Data availability

The raw/processed data required to reproduce these findings cannot be shared at this time as the data also forms part of an ongoing study.

CRediT authorship contribution statement

Mustafa Güden: Conceptualization, Validation, Formal analysis, Resources, Writing – original draft, Writing – review & editing. **Hakan Yavaş:** Conceptualization, Validation, Resources. **Ahmet Alptuğ Tanrıkulu:** Investigation, Resources. **Alper Taşdemirci:** Conceptualization, Validation, Writing – original draft, Writing – review & editing. **Barış Akın:** Investigation. **Samed Enser:** Methodology, Formal analysis, Investigation, Writing – original draft. **Ayberk Karakuş:** Methodology. **Burcu Arslan Hamat:** Methodology, All authors have read and agreed to the published version of the manuscript.

Declaration of competing interest

The authors declare that they have no known competing financial

interests or personal relationships that could have appeared to influence the work reported in this paper.

Appendix A. Supplementary data

Supplementary data to this article can be found online at https://doi.org/10.1016/j.msea.2021.141808.

References

[1] H.A. Parr G, An Introduction to Stainless Steel, ASM, Materials Park, 1965.
[2] N. Haghdadi, M. Laleh, M. Moyle, S. Primig, Additive manufacturing of steels: a review of achievements and challenges, J. Mater. Sci. 56 (1) (2021) 64–107.
[3] P. Bajaj, A. Hariharan, A. Kini, P. Kurnsteiner, D. Raabe, E.A. Jagle, Steels in additive manufacturing: a review of their microstructure and properties, Mater, Sci. Eng. A-Struct. Mater. Prop. Microstruct. Process. 772 (2020) 25.
[4] X. Zhang, C.J. Yocom, B. Mao, Y.L. Liao, Microstructure evolution during selective laser melting of metallic materials: a review, J. Laser Appl. 31 (3) (2019) 19.
[5] B. Song, X. Zhao, S. Li, C. Han, Q. Wei, S. Wen, J. Liu, Y. Shi, Differences in microstructure and properties between selective laser melting and traditional manufacturing for fabrication of metal parts: a review, Front. Mech. Eng. 10 (2) (2015) 111–125.
[6] L.-E. Loh, C.-K. Chua, W.-Y. Yeong, J. Song, M. Mapar, S.-L. Sing, Z.-H. Liu, D.-Q. Zhang, Numerical investigation and an effective modelling on the Selective Laser Melting (SLM) process with aluminium alloy 6061, Int. J. Heat Mass Tran. 80 (2015) 288–300.
[7] P. Mercelis, J.P. Kruth, Residual stresses in selective laser sintering and selective laser melting, Rapid Prototyp. J. 12 (5) (2006) 254–265.
[8] Z.C. Fang, Z.L. Wu, C.G. Huang, C.W. Wu, Review on residual stress in selective laser melting additive manufacturing of alloy parts, Opt Laser. Technol. 129 (2020) 15.
[9] T. Kim, K. Ha, Y.R. Cho, J.B. Jeon, W. Lee, Analysis of residual stress evolution during powder bed fusionprocess of AISI 316L stainless steel with experiment and numerical modeling, Int. J. Adv. Manuf. Technol. 105 (1–4) (2019) 309–323.
[10] H. Fayazfar, M. Salarian, A. Rogalsky, D. Sarker, P. Russo, V. Paserin, E. Toyserkani, A critical review of powder-based additive manufacturing of ferrous alloys: process parameters, microstructure and mechanical properties, Mater. Des. 144 (2018) 98–128.
[11] J.J. Lewandowski, M. Seifi, Metal additive manufacturing: a review of mechanical properties, in: D.R. Clarke (Ed.), Annual Review of Materials Research, vol. 46, Annual Reviews, Palo Alto, 2016, pp. 151–186.
[12] K. Saeidi, X. Gao, Y. Zhong, Z.J. Shen, Hardened austenite steel with columnar sub-grain structure formed by laser melting, Mater. Sci. Eng. A-Struct. Mater. Prop. Microstruct. Process. 625 (2015) 221–229.
[13] Y. Zhong, L.F. Liu, S. Wikman, D.Q. Cui, Z.J. Shen, Intragranular cellular segregation network structure strengthening 316L stainless steel prepared by selective laser melting, J. Nucl. Mater. 470 (2016) 170–178.
[14] M. Zietala, T. Durejko, M. Polanski, I. Kunce, T. Plocinski, W. Zielinski, M. Lazinska, W. Stepniowski, T. Czujko, K.J. Kurzydlowski, Z. Bojar, The microstructure, mechanical properties and corrosion resistance of 316 L stainless steel fabricated using laser engineered net shaping, Mater. Sci. Eng. A-Struct. Mater. Prop. Microstruct. Process. 677 (2016) 1–10.
[15] S. Gorsse, C. Hutchinson, M. Goune, R. Banerjee, Additive manufacturing of metals: a brief review of the characteristic microstructures and properties of steels, Ti-6Al-4V and high-entropy alloys, Sci. Technol. Adv. Mater. 18 (1) (2017) 584–610.
[16] M.-S. Pham, P. Hooper, Roles of microstructures on deformation response of 316 stainless steel made by 3D printing, AIP Conference Proceedings 1896 (1) (2017), 040017.
[17] M.S. Pham, B. Dovgyy, P.A. Hooper, Twinning induced plasticity in austenitic stainless steel 316L made by additive manufacturing, Mater. Sci. Eng. A-Struct. Mater. Prop. Microstruct. Process. 704 (2017) 102–111.
[18] Y.M. Wang, T. Voisin, J.T. McKeown, J. Ye, N.P. Calta, Z. Li, Z. Zeng, Y. Zhang, W. Chen, T.T. Roehling, R.T. Ott, M.K. Santala, Philip J. Depond, M.J. Matthews, A. V. Hamza, T. Zhu, Additively manufactured hierarchical stainless steels with high strength and ductility, Medium: X; Size (2017) 63–71.
[19] Y.J. Yin, J.Q. Sun, J. Guo, X.F. Kan, D.C. Yang, Mechanism of high yield strength and yield ratio of 316 L stainless steel by additive manufacturing, Mater. Sci. Eng. A-Struct. Mater. Prop. Microstruct. Process. 744 (2019) 773–777.
[20] X.L. Wang, J.A. Muniz-Lerma, M.A. Shandiz, O. Sanchez-Mata, M. Brochu, Crystallographic-orientation-dependent tensile behaviours of stainless steel 316L fabricated by laser powder bed fusion, Mater. Sci. Eng. A-Struct. Mater. Prop. Microstruct. Process. 766 (2019) 16.
[21] M.M. Ma, Z.M. Wang, X.Y. Zeng, A comparison on metallurgical behaviors of 316L stainless steel by selective laser melting and laser cladding deposition, Mater. Sci. Eng. A-Struct. Mater. Prop. Microstruct. Process. 685 (2017) 265–273.
[22] Z. Sun, X. Tan, S.B. Tor, C.K. Chua, Simultaneously enhanced strength and ductility for 3D-printed stainless steel 316L by selective laser melting, NPG Asia Mater. 10 (4) (2018) 127–136.
[23] S.-H. Sun, T. Ishimoto, K. Hagihara, Y. Tsutsumi, T. Hanawa, T. Nakano, Excellent mechanical and corrosion properties of austenitic stainless steel with a unique crystallographic lamellar microstructure via selective laser melting, Scripta Mater. 159 (2019) 89–93.
[24] T. Niendorf, S. Leuders, A. Riemer, F. Brenne, T. Tröster, H.A. Richard, D. Schwarze, Functionally graded alloys obtained by additive manufacturing, Adv. Eng. Mater. 16 (7) (2014) 857–861.
[25] O. Andreau, I. Koutiri, P. Peyre, J.-D. Penot, N. Saintier, E. Pessard, T. De Terris, C. Dupuy, T. Baudin, Texture control of 316L parts by modulation of the melt pool morphology in selective laser melting, J. Mater. Process. Technol. 264 (2019) 21–31.
[26] T. Niendorf, S. Leuders, A. Riemer, H.A. Richard, T. Tröster, D. Schwarze, Highly anisotropic steel processed by selective laser melting, Metall. Mater. Trans. B 44 (4) (2013) 794–796.
[27] W. Woo, J.S. Jeong, D.K. Kim, C.M. Lee, S.H. Choi, J.Y. Suh, S.Y. Lee, S. Harjo, T. Kawasaki, stacking fault energy analyses of additively manufactured stainless steel 316L and CrCoNi medium entropy alloy using in situ neutron diffraction, Sci. Rep. 10 (1) (2020) 15.
[28] L.F. Liu, Q.Q. Ding, Y. Zhong, J. Zou, J. Wu, Y.L. Chiu, J.X. Li, Z. Zhang, Q. Yu, Z. J. Shen, Dislocation network in additive manufactured steel breaks strength-ductility trade-off, Mater. Today 21 (4) (2018) 354–361.
[29] A. Rottger, K. Geenen, M. Windmann, F. Binner, W. Theisen, Comparison of microstructure and mechanical properties of 316 L austenitic steel processed by selective laser melting with hot-isostatic pressed and cast material, Mater. Sci. Eng. A-Struct. Mater. Prop. Microstruct. Process. 678 (2016) 365–376.
[30] U. Department of Defense, Fastener Test Methods, Method 13, Double Shear Test MIL-STD-1312-13a, 1991.
[31] B. Beausir, J.-J. Fundenberger, Analysis Tools for Electron and X-Ray Diffraction, ATEX - software, 2017. www.atex-software.eu.
[32] C. Suryanarayana, M. Grant Norton, X-Ray Diffraction: A Practical Approach, Springer, New York, 1998.
[33] G.K. Williamson, R.E. Smallman III., Dislocation densities in some annealed and cold-worked metals from measurements on the X-ray debye-scherrer spectrum, Phil. Mag.: A Journal of Theoretical Experimental and Applied Physics 1 (1) (1956) 34–46.
[34] G.I. Taylor, The mechanism of plastic deformation of crystals. Part I. Theoretical, Proc. R. Soc. Lond. - Ser. A Contain. Pap. a Math. Phys. Character 145 (855) (1934) 362–387.
[35] B.B. He, B. Hu, H.W. Yen, G.J. Cheng, Z.K. Wang, H.W. Luo, M.X. Huang, High dislocation density–induced large ductility in deformed and partitioned steels, Science 357 (6355) (2017) 1029–1032.
[36] T.S. Byun, On the stress dependence of partial dislocation separation and deformation microstructure in austenitic stainless steels, Acta Mater. 51 (11) (2003) 3063–3071.
[37] S.W. Tsai, Strength Theories of Filamentary Structures Fundamental Aspects of Fiber Reinforced Plastic Composites, Wiley-Interscience, New York, 1968.
[38] Z. Li, T. Voisin, J.T. McKeown, J.C. Ye, T. Braun, C. Kamath, W.E. King, Y.M. Wang, Tensile properties, strain rate sensitivity, and activation volume of additively manufactured 316L stainless steels, Int. J. Plast. 120 (2019) 395–410.
[39] F. Stern, J. Kleinhorst, J. Tenkamp, F. Walther, Investigation of the anisotropic cyclic damage behavior of selective laser melted AISI 316L stainless steel, Fatig. Fract. Eng. Mater. Struct. 42 (11) (2019) 2422–2430.
[40] J.J. Marattukalam, D. Karlsson, V. Pacheco, P. Beran, U. Wiklund, U. Jansson, B. Hjorvarsson, M. Sahlberg, The effect of laser scanning strategies on texture, mechanical properties, and site-specific grain orientation in selective laser melted 316L SS, Mater. Des. 193 (2020) 11.
[41] M. Shamsujjoha, S.R. Agnew, J.M. Fitz-Gerald, W.R. Moore, T.A. Newman, High strength and ductility of additively manufactured 316L stainless steel explained, Metall. Mater. Trans. A-Phys. Metall. Mater. Sci. 49A (7) (2018) 3011–3027.
[42] S. Morito, J. Nishikawa, T. Maki, Dislocation density within lath martensite in Fe-C and Fe-Ni alloys, ISIJ Int. 43 (9) (2003) 1475–1477.
[43] J.W. Christian, S. Mahajan, Deformation twinning, Prog. Mater. Sci. 39 (1–2) (1995) 1–157.
[44] T. Mukherjee, W. Zhang, T. DebRoy, An improved prediction of residual stresses and distortion in additive manufacturing, Comput. Mater. Sci. 126 (2017) 360–372.
[45] A. Keshavarzkermani, M. Sadowski, L. Ladani, Direct metal laser melting of Inconel 718: process impact on grain formation and orientation, J. Alloys Compd. 736 (2018) 297–305.
[46] L. Ladani, Local and global mechanical behavior and microstructure of Ti6Al4V parts built using electron beam melting technology, Metall. Mater. Trans. 46 (9) (2015) 3835–3841.
[47] L. Ladani, J. Razmi, S. Farhan Choudhury, Mechanical anisotropy and strain rate dependency behavior of Ti6Al4V produced using E-beam additive fabrication, J. Eng. Mater. Technol. 136 (3) (2014), 031006.
[48] A. Mertens, S. Reginster, Q. Contrepois, T. Dormal, O. Lemaire, J. Lecomte-Beckers, Microstructures and mechanical properties of stainless steel AISI 316L processed by selective laser melting, Mater. Sci. Forum 783–786 (2014) 898–903.
[49] M. Shamsujjoha, S.R. Agnew, J.M. Fitz-Gerald, W.R. Moore, T.A. Newman, High strength and ductility of additively manufactured 316L stainless steel explained, Metall. Mater. Trans. 49 (7) (2018) 3011–3027.
[50] X. Wang, J.A. Muñiz-Lerma, O. Sánchez-Mata, M. Attarian Shandiz, M. Brochu, Microstructure and mechanical properties of stainless steel 316L vertical struts manufactured by laser powder bed fusion process, Mater. Sci. Eng., A 736 (2018) 27–40.
[51] A.J. Birnbaum, H. Ryou, J.C. Steuben, A.P. Iliopoulos, K.J. Wahl, J.G. Michopoulos, Nested size effects in the nanoindentation response of additively manufactured 316L stainless steel, Mater. Lett. 280 (2020) 128570.
[52] R.H. Morgan, A.J. Papworth, C. Sutcliffe, P. Fox, W. O'Neill, J. Mater. Sci. 37 (15) (2002) 3093–3100.

[53] W. Di, Y. Yongqiang, S. Xubin, C. Yonghua, Study on energy input and its influences on single-track,multi-track, and multi-layer in SLM, Int. J. Adv. Manuf. Technol. 58 (9–12) (2012) 1189–1199.
[54] D. Hagedorn-Hansen, M. Bezuidenhout, D. Dimitrov, T. Oosthuizen, The effects OF selective laser melting scan strategies ON deviation OF hybrid parts, S. Afr. J. Ind. Eng. 28 (3) (2017).
[55] L. Rémy, A. Pineau, Twinning and strain-induced f.c.c. → h.c.p. transformation on the mechanical properties of Co-Ni-Cr-Mo alloys, Mater. Sci. Eng. 26 (1) (1976) 123–132.
[56] A.H. Cottrell, Theory of dislocations, Prog. Met. Phys. 4 (1953) 205–264.
[57] I. Karaman, H. Sehitoglu, K. Gall, Y.I. Chumlyakov, On the deformation mechanisms in single crystal hadfield manganese steels, Scripta Mater. 38 (6) (1998) 1009–1015.
[58] S.M. Copley, B.H. Kear, The dependence of the width of a dissociated dislocation on dislocation velocity, Acta Metall. 16 (2) (1968) 227–231.
[59] I.V. Kireeva, Y.I. Chumlyakov, Z.V. Pobedennaya, I.V. Kuksgausen, I. Karaman, Orientation dependence of twinning in single crystalline CoCrFeMnNi high-entropy alloy, Mater. Sci. Eng., A 705 (2017) 176–181.
[60] G. Meric De Bellefon, J.C. Van Duysen, K. Sridharan, Composition-dependence of stacking fault energy in austenitic stainless steels through linear regression with random intercepts, J. Nucl. Mater. 492 (2017) 227–230.
[61] S. Mahajan, D.F. Williams, Deformation twinning in metals and alloys, Int. Metall. Rev. 18 (2) (1973) 43–61.
[62] I. Karaman, H. Sehitoglu, K. Gall, Y.I. Chumlyakov, H.J. Maier, Deformation of single crystal Hadfield steel by twinning and slip, Acta Mater. 48 (6) (2000) 1345–1359.
[64] ANSYS 2020 R1. Mechanical User's Guide, ANSYS Inc, Canonsburg, USA, 2020.
[65] LSTC, LS-DYNA R11: Keyword User's Manual, Livermore Software Technology Corporation, LSTC, 2018.